Journal of Magnetic Resonance **157,** 92–105 (2002)
doi:10.1006/jmre.2002.2582

Effects of Restricted Diffusion on MR Signal Formation

Alexander L. Sukstanskii and Dmitriy A. Yablonskiy[1]

Mallinckrodt Institute of Radiology, Washington University School of Medicine, 4525 Scott Avenue, St. Louis, Missouri 63110

Received February 19, 2002; revised June 10, 2002; published online August 5, 2002

Numerous functional MRI (fMRI) and diffusion MR studies have recently boosted interest in the theory of MR signal formation in biological systems in the presence of mesoscopic magnetic field inhomogeneities. Herein we report an exact solution to the problem of free induction decay (FID) and spin echo (SE) signal formation in the presence of a constant field gradient in three models of one-, two-, and three-dimensional restricted diffusion. We demonstrate the transition with increasing diffusion coefficient from the oscillating FID signal behavior in the static dephasing regime to a monotonic exponential behavior in the motional narrowing regime. Quantitative criteria are presented for applicability of the Gaussian approximation for the description of the MR signal. The spatial distribution of signal density and the edge enhancement effect are analyzed. We also demonstrate that the presence of restrictive barriers in a one-compartment model can lead to a quasi-two-compartment behavior of the MR signal. This result suggests a simple rationale for the experimental findings of biexponential echo attenuation curves in MR diffusion experiments with tissue systems. © 2002 Elsevier Science (USA)

Key Words: **magnetic resonance; MRI; fMRI; relaxation effects; diffusion MR.**

1. INTRODUCTION

The presence of magnetic field inhomogeneities is known to play a significant role in the process of magnetic resonance (MR) signal decay. If such inhomogeneities are absent, the MR signal is attenuated mainly by the irreversible transverse relaxation processes described by the relaxation time constant T_2. An inhomogeneous magnetic field results in dephasing of nuclear spin precession and therefore opens additional channels for the MR signal decay. In application to MR imaging, the magnetic inhomogeneities on the mesoscopic scale (much smaller than the voxel size but much bigger than the atomic and molecular scale) are of special interest because they orginate from internal, tissue-specific sources, and hence can provide important information of biological tissue structure and function.

In earlier works, attention was concentrated on the SE signal evolution (see, e.g., monographs (*1, 2*) and numerous references therein). Functional MRI (fMRI) studies in biology and medicine initiated in (*3*) have recently boosted interest in FID-type experiments. For example, in the case of fMRI, paramagnetic deoxyhemoglobin in venous blood creates a mesoscopic inhomogeneous magnetic field in the tissue surrounding the blood vessel network, leading to FID signal dephasing dependent upon blood oxygenation level (BOLD contrast). This phenomenon has been broadly used to detect changes in brain activity.

A comprehensive analytical approach for calculating the FID signal in the presence of mesoscopic field inhomogeneities was developed in (*4, 5*) for the static dephasing regime, when diffusion of the spins is negligible. In (*6*) the effect of diffusion on the FID signal dephasing in a microvascular network was studied in the slow-diffusion limit and in (*7*) in the motional narrowing regime. Analytical approximations relying on the assumption of a Gaussian distribution of phases accumulated by the precessing spins and simple phenomenological exponential spin correlation functions in the presence of mesoscopic field gradients were proposed in (*8*) and further developed in (*9*). Numerical calculations of the FID signal behavior in the presence of mesoscopic field gradients were performed in a number of studies (see, e.g., (*10–12*)).

In principle, the FID signal can be calculated by solving the Bloch–Torrey equation (*13*). An exact solution for the case of unrestricted diffusion with an arbitrary initial spin distribution and arbitrary time dependence of a field gradient was found in Ref. (*14*). However, a direct integration of this equation even in the simplest one-dimensional model of restricted diffusion in the presence of a constant field gradient faces substantial mathematical difficulties. The only known explicit analytical solution was found for a semi-infinite interval in Ref. (*15*), where for the case of diffusion between two boundaries, the Laplace transform of the Green's function of the Bloch–Torrey equation was also obtained.

A rather powerful approach for the calculation of the MR signal in the presence of external magnetic field gradients has been proposed in (*16*) in conjunction with studies of restricted diffusion. This approach is based on dividing the gradient pulse into successive short time intervals and then using a propagator for each stage of the evolution—the so-called "multiple propagator approach." In Ref. (*17*) this method was reformulated in a simple-to-use form, which enables calculation of the signal as a product of matrices. As demonstrated in (*16, 17*) for

[1] To whom correspondence should be addressed. E-mail: yablonskiyd@mir.wustl.edu.

1090-7807/02 $35.00
© 2002 Elsevier Science (USA)
All rights reserved.

one-dimensional diffusion and in (*18*) for cylindrical and spherical geometries, the multiple propagator approach provides a very good approximation for the SE signal as verified by comparison with previous Monte Carlo simulations (*19–22*).

In the present paper we apply a method similar to the multiple propagator approach to describe the FID and SE signal behavior, exemplifying it by three classical models: (i) one-dimensional (1D) model, in which diffusion is restricted by two parallel infinite planes with the field gradient applied normal to the planes; in this case, only diffusion along the normal affects the signal; (ii) 2D model, in which spins diffuse in an infinite cylinder, the field gradient being applied perpendicular to the cylinder axis; only diffusion in the basal plane affects the signal; (iii) 3D model, with spins diffusing in a sphere. All boundaries are supposed to be reflecting and nondepolarizing. We show how the static dephasing-like oscillating time dependence of the FID signal transforms with increasing diffusion coefficient to the monotonic exponential decay in the motional narrowing regime. Quantitative conditions of applicability of the Gaussian approximation for describing the FID and SE signals are found. A spatial distribution of signal density and the edge enhancement effect are analyzed. We also demonstrate that the presence of restrictive barriers in a one-compartment model can result in a quasi-two-compartment behavior of MR signal. This result might contribute to explanation of experimental findings (see, e.g., (*23–28*)) of biexponential diffusion attenuation.

2. RANDOM WALK APPROACH

In the general case, the signal produced by a system of a large number of precessing spins at time t after RF pulse is

$$S(t) = S_0(t)\, s(t), \qquad s(t) = \langle \exp[i\varphi(t)] \rangle, \qquad [1]$$

where the factor $S_0(t)$ describes the signal time dependence in the absence of diffusion-sensitizing gradients and accounts for the transverse T_2 relaxation, $\varphi(t)$ is the phase accumulated by a single spin by time t, and $\langle \cdots \rangle$ means averaging over all possible initial positions and trajectories. In an inhomogeneous magnetic field, $\mathbf{H} = \mathbf{H}(\mathbf{r}, t)$, the phase $\varphi(t)$ of the spin moving along a given trajectory $\mathbf{r} = \mathbf{r}(t)$ can be written as

$$\varphi(t) = \int_0^t dt'\, \omega(\mathbf{r}(t'), t'), \qquad [2]$$

where the Larmor frequency $\omega = \gamma \mathbf{H}$. The phase in Eq. [2] depends on all the points of the trajectory.

Following the well known procedure for numerical calculation of integrals, we divide the spin's trajectory into n small intervals Δt, $t = N \cdot \Delta t$, and use the trapezoidal approximation,

$$\varphi(t) \simeq \Delta t \cdot \left[\frac{\omega(\mathbf{r}_0, 0) + \omega(\mathbf{r}_N, t)}{2} + \sum_{n=1}^{N-1} \omega(\mathbf{r}_n, t_n) \right], \qquad [3]$$

where $t_n = n \cdot \Delta t$ and $\mathbf{r}_n = \mathbf{r}(t_n)$ are points successively passed by the spin. Note that the Larmor frequency depends on time both explicitly (due to the time dependence of the magnetic field) and implicitly (due to the motion). In what follows, we restrict ourselves to considering diffusion in a constant field gradient, $\mathbf{H} = \mathbf{G} \cdot \mathbf{r}$, $\mathbf{G} = \text{const}$. In this case, only the implicit time dependence of the Larmor frequency is present and the phase can be written in the form

$$\varphi(t) = \gamma \mathbf{G}\, \Delta t \left(\frac{\mathbf{r}_0 + \mathbf{r}_N}{2} + \sum_{n=1}^{N-1} \mathbf{r}_n \right). \qquad [4]$$

The phase [4] corresponds to a specific spin's trajectory. To obtain the signal, we should further average the signal $\exp(i\varphi(t))$ over all possible trajectories. We introduce the probability of the spin starting at point $\mathbf{r}_0$ and successively passing the points $\mathbf{r}_1$, $\mathbf{r}_2, \ldots, \mathbf{r}_N$ at times $t_1, t_2, \ldots, t_N$. This probability is a product

$$\rho(\mathbf{r}_0) \cdot P(\mathbf{r}_1, \mathbf{r}_0, \Delta t) \cdot P(\mathbf{r}_2, \mathbf{r}_1, \Delta t) \cdot \ldots \cdot P(\mathbf{r}_N, \mathbf{r}_{N-1}, \Delta t), \qquad [5]$$

where $\rho(\mathbf{r}_0)$ is the initial spin distribution (for the homogeneous distribution, $\rho(\mathbf{r}_0) = 1/V$, where V is the system volume) and $P(\mathbf{r},\ \mathbf{r}',\ \Delta t)$ is the propagator determining the probability that a particle starting at the point $\mathbf{r}'$ moves to the point $\mathbf{r}$ during the time interval Δt. In the random walk approximation, the propagator $P(\mathbf{r},\ \mathbf{r}',\ \Delta t)$ satisfies the diffusion equation

$$\frac{\partial P}{\partial t} = D \nabla^2 P \qquad [6]$$

with the initial condition, $P(\mathbf{r}, \mathbf{r}', 0) = \delta(\mathbf{r} - \mathbf{r}')$ (here $\delta(\mathbf{r})$ is the Dirac delta function), and boundary conditions specified for the system under consideration.

Substituting Eqs. [4]–[5] in Eq. [1], we obtain the net signal produced by the diffusing spins,

$$s = \frac{1}{V} \int_V d\mathbf{r}_0 \int_V d\mathbf{r}_1 \cdots \int_V d\mathbf{r}_N \exp\left[i\mathbf{Q} \left(\frac{\mathbf{r}_0 + \mathbf{r}_N}{2} + \mathbf{r}_1 + \mathbf{r}_2 + \cdots + \mathbf{r}_{N-1} \right) \right] \cdot P(\mathbf{r}_1, \mathbf{r}_0, \Delta t) \times P(\mathbf{r}_2, \mathbf{r}_1, \Delta t) \cdots P(\mathbf{r}_N, \mathbf{r}_{N-1}, \Delta t), \qquad [7]$$

where $\mathbf{Q} = \gamma \mathbf{G} \cdot \Delta t$.

Because it is the Green's function of the diffusion equation [6], the propagator $P(\mathbf{r},\ \mathbf{r}',\ t)$ allows the standard expansion in terms of the orthogonal set of eigenfunctions $\{u_k(\mathbf{r}),\ k = 0, 1, 2, \ldots\}$ of the Sturm–Liouville problem for the geometry under consideration,

$$P(\mathbf{r}, \mathbf{r}', t) = \frac{1}{V} \sum_{k=0}^{\infty} u_k(\mathbf{r}) u_k^*(\mathbf{r}') \exp(-\lambda_k t), \qquad [8]$$

where the λ_k are the corresponding eigenvalues. The functions $u_k(\mathbf{r})$ are orthogonal to each other and satisfy the normalization conditions

$$\frac{1}{V}\int_V d\mathbf{r}|u_k(\mathbf{r})|^2 = 1. \quad [9]$$

Substituting expansion [8] in Eq. [7], after some rearrangements, we obtain

$$s(t) = \sum_{k_1 k_2,\ldots,k_N} F_{k_1}\left(\frac{\mathbf{Q}}{2}\right)\Lambda_{k_1k_1}U_{k_1k_2}(\mathbf{Q})\,\Lambda_{k_2k_2}U_{k_2k_3}(\mathbf{Q}) \times \Lambda_{k_3k_3}\cdots U_{k_{N-1}k_N}(\mathbf{Q})\Lambda_{k_Nk_N}F^*_{k_N}\left(-\frac{\mathbf{Q}}{2}\right), \quad [10]$$

where

$$F_k(\mathbf{Q}) = \frac{1}{V}\int_V d\mathbf{r}\,u_k(\mathbf{r})\exp(i\mathbf{Qr}) \quad [11]$$

$$\Lambda_{kk} = \exp(-\lambda_k\,\Delta t) \quad [12]$$

$$U_{kk'} = \frac{1}{V}\int_V d\mathbf{r}\,u^*_k(\mathbf{r})u_{k'}(\mathbf{r})\exp(i\mathbf{Qr}). \quad [13]$$

Introducing the row vector $\mathbf{F} = \{F_k\}$, the matrix $\hat{\mathbf{U}} = \{U_{kk'}\}$, and the diagonal matrix $\hat{\Lambda} = diag\{\Lambda_{kk}\}$, the expression [10] can be written as a matrix product

$$s(t) = \mathbf{F}\left(\frac{\mathbf{Q}}{2}\right)\cdot\hat{\mathbf{\Lambda}}(\Delta t)\cdot[\hat{\mathbf{U}}(\mathbf{Q})\cdot\hat{\mathbf{\Lambda}}(\Delta t)]^{N-1}\cdot\mathbf{F}^\dagger\left(-\frac{\mathbf{Q}}{2}\right), \quad [14]$$

where $\mathbf{F}^\dagger$ is the Hermitian conjugate of $\mathbf{F}$.

An expression similar to Eq. [14] can be readily obtained (as the particular case $\mathbf{G}(t) = \text{const}$) from the general expression for an arbitrary gradient waveform given in Ref. (*17*) in the framework of the multiple propagator approach. The minor difference is in the arguments of the vector elements $\mathbf{F}$. However, though the mathematical structures of both approaches are very similar, our approach is based on the very transparent physical picture of the random walk description of diffusion. Therefore we refer to our approach as the random walk approach (RWA).

The matrix form of the expressions [14]–[18] for the signal substantially facilitates its calculation, which can be performed by means of any matrix-handling tools like *Mathematica* or *MatLab*. For this purpose we should choose an appropriate time step Δt and a number of eigenfunctions involved in the expansion [8] (the dimensionality M of the matrices $\hat{\mathbf{U}}$ and $\hat{\mathbf{\Lambda}}$). As the matrix elements Λ_{kk} [12] decrease exponentially with λ_k, it is possible to restrict M to some comparably small value determined by the precision criteria (see below).

Our approach allows us to not only find out the net signal but also calculate a signal density $\sigma = \sigma(\mathbf{r}, t)$ produced by all spins starting from a given space point $\mathbf{r}$ as well as a signal density $\sigma' = \sigma'(\mathbf{r}, t)$ produced from a given point of the system, i.e., by all spins ending their trajectories at a point $\mathbf{r}$ at a time t. The density $\sigma(\mathbf{r}, t)$ can be readily calculated by averaging a phase [4] over all trajectories starting at a point $\mathbf{r}_0$ without integration over $\mathbf{r}_0$ in Eq. [7]. Similarly, to calculate the signal density $\sigma'(\mathbf{r}, t)$, integration over the final point of spin trajectory $\mathbf{r}_N$ should be eliminated in Eq. [7]. As a result, the signal densities $\sigma(\mathbf{r}, t)$ and $\sigma'(\mathbf{r}, t)$ can be written in the form

$$\sigma(\mathbf{r}, t) = \boldsymbol{\varphi}\left(\mathbf{r}, \frac{\mathbf{Q}}{2}\right)\cdot\hat{\mathbf{\Lambda}}(\Delta t)\cdot[\hat{\mathbf{U}}(\mathbf{Q})\cdot\hat{\mathbf{\Lambda}}(\Delta t)]^{N-1}\cdot\mathbf{F}^\dagger\left(-\frac{\mathbf{Q}}{2}\right), \quad [15]$$

$$\sigma'(\mathbf{r}, t) = \mathbf{F}\left(\frac{\mathbf{Q}}{2}\right)\cdot\hat{\mathbf{\Lambda}}(\Delta t)\cdot[\hat{\mathbf{U}}(\mathbf{Q})\cdot\hat{\mathbf{\Lambda}}(\Delta t)]^{N-1}\cdot\boldsymbol{\varphi}^\dagger\left(\mathbf{r}, -\frac{\mathbf{Q}}{2}\right), \quad [16]$$

where the elements of the vector $\boldsymbol{\varphi}$ are

$$\phi_k(\mathbf{r}, \mathbf{Q}) = \frac{1}{V}u_k(\mathbf{r})\exp(i\mathbf{Qr}). \quad [17]$$

It is easy to see that $\sigma(\mathbf{r}, t) = \sigma'(\mathbf{r}, t)$. In addition, the function $\sigma(\mathbf{r}, t)$ can be proved to be an exact solution to the Bloch–Torrey equation (*13*) (the proof will be published elsewhere).

The expression [14] corresponds to the FID signal. A similar expression for the SE signal with the echo time t can be written in the form

$$s_{SE}(t) = \hat{\mathbf{T}}\hat{\mathbf{T}}^\dagger, \qquad \hat{\mathbf{T}} = \mathbf{F}\left(\frac{\mathbf{Q}}{2}\right)\cdot\hat{\mathbf{\Lambda}}(\Delta t)\cdot[\hat{\mathbf{U}}(\mathbf{Q})\cdot\hat{\mathbf{\Lambda}}(\Delta t)]^{N/2-1}. \quad [18]$$

As mentioned in the Introduction, we will compare the results of RWA with those obtained in the Gaussian approximation. In this approximation, the signal is calculated by means of the phase distribution function $P(\varphi, t)$, which is assumed to be Gaussian (with zero mean value, $\langle\varphi(t)\rangle = 0$) (*29, 30*),

$$P(\varphi, t) = \frac{1}{(2\pi\langle\varphi^2(t)\rangle)^{1/2}}\exp\left[-\frac{\varphi^2}{2\langle\varphi^2(t)\rangle}\right]. \quad [19]$$

The signal in the Gaussian approximation is equal to

$$s(t) = \int d\varphi\,P(\varphi, t)\exp(i\varphi) = \exp\left[-\frac{\langle\varphi^2(t)\rangle}{2}\right]. \quad [20]$$

For the signal in the presence of the field gradient $\mathbf{G}(t)$, the quantity $\langle\varphi^2(t)\rangle$ can be written in the form

$$\langle\varphi^2(t)\rangle = \frac{2\gamma^2}{V}\int_0^t dt_1\int_0^{t_1} dt_2\int_V d\mathbf{r}_1\int_V d\mathbf{r}_2(\mathbf{G}(t_1)\mathbf{r}_1) \times(\mathbf{G}(t_2)\mathbf{r}_2)P(\mathbf{r}_1, \mathbf{r}_2, t_1 - t_2). \quad [21]$$

In the case of FID signal, $\mathbf{G}(t) = \text{const}$. The case of SE signal can be described by changing the gradient sign at $t/2$.

3. THE 1D MODEL

In the simplest case of one-dimensional diffusion, in which the spins are distributed between two nondepolarizing, reflecting, infinite parallel planes localized at positions $x = 0$ and $x = 2a$, a solution to the diffusion equation [6] with boundary conditions $\partial P/\partial x_{|x=0} = \partial P/\partial x_{|x=2a} = 0$ is well known (see, e.g., (*31*)) and is given by Eq. [8] with

$$\lambda_k = \frac{D\beta_k^2}{a^2}, \qquad \beta_k = \frac{\pi k}{2} \tag{22}$$

and the eigenfunctions

$$u_k(x) = \eta_k \cos\frac{\pi k x}{2a}, \tag{23}$$

where the normalization factors are $\eta_0 = 1$ and $\eta_k = \sqrt{2}$ for $k \neq 0$.

For the constant field gradient symmetric with respect to the center of the interval, $H = G(x - a)$, we readily obtain the components of the vector $\mathbf{F}$ and of the matrix $\hat{\mathbf{U}}$,

$$F_k = \eta_k f_k, \qquad U_{kk'} = \frac{\eta_k \eta_{k'}}{2}\left[f_{k+k'} + f_{|k-k'|}\right], \tag{24}$$

$$f_k = \frac{2i\Phi}{[(\pi k)^2 - 4\Phi^2]}[-\exp(-i\Phi) + (-1)^k \exp(i\Phi)], \qquad \Phi = Qa = \gamma G a\, \Delta t. \tag{25}$$

There are two characteristic time parameters in the model, determining the signal behavior: the diffusion time t_D, which determines the time needed for a spin to diffuse over the system size a, and the dephasing time t_c, which defines the time of signal dephasing in the absence of diffusion,

$$t_D \equiv \frac{a^2}{D}, \qquad t_c \equiv \frac{1}{\gamma G a}. \tag{26}$$

If we measure time in the units of one of these characteristic times, for example, t_c, the FID signal dependence on $\tau = t/t_c$ will be governed by the sole dimensionless parameter

$$p = \frac{t_c}{t_D} = \frac{D}{\gamma G a^3}. \tag{27}$$

The parameter Φ in Eq. [25] and the elements of the matrix $\hat{\mathbf{\Lambda}}$ [12] are equal to

$$\Phi = \Delta\tau \equiv \frac{\Delta t}{t_c}, \qquad \Lambda_{kk} = \exp\left(-\beta_k^2 p \cdot \Delta\tau\right). \tag{28}$$

The dimensionless time τ and the parameter p are similar to the parameter $qa = \gamma G a \delta/2\pi$ (δ is the length of the gradient pulses in pulse-gradient SE experiments) and the inverse "dimensionless gradient" used in Refs. (*16, 17, 21*), respectively.

If diffusion is absent ($p = 0$), the signal $s(\tau)$ in the one-dimensional system under consideration is described by the well known *sinc*-function expression,

$$s(t) = \text{sinc}(\tau) = \frac{\sin\tau}{\tau}, \qquad p = 0 \tag{29}$$

(this result can be trivially derived directly from the general expressions [1]–[2]).

The expression for the FID signal for one-dimensional restricted diffusion obtained in the framework of the Gaussian approximation (marked below by the upper index (G)) can be easily obtained from Eqs. [20]–[21],

$$s^{(G)}(\tau) = \exp\left[-\frac{2}{p^2}\sum_{k=1}^{\infty}\frac{g\left(p\beta_{2k-1}^2\tau\right)}{\beta_{2k-1}^8}\right], \tag{30}$$

where the function $g(x)$ is

$$g(x) = \exp(-x) + x - 1. \tag{31}$$

The SE signal in the Gaussian approximation is described by Eq. [30], in which the function $g(x)$ should be substituted by the function $\bar{g}(x)$ (see, e.g., (*29, 30*)),

$$g(x) \to \bar{g}(x) = x - 3 + 4\exp(-x/2) - \exp(-x). \tag{32}$$

4. THE 2D MODEL

The solution of the two-dimensional diffusion equation [6] within a circle of radius a, satisfying the boundary condition $(\partial P/\partial\rho)_{|\rho=a} = 0$, can be written in the form [8] with the eigenfunctions (*31*)

$$u_k(\boldsymbol{\rho}, t) \equiv u_{n\mu}(\boldsymbol{\rho}, t) = \eta_{n\mu} J_n\left(\beta_{n\mu}\frac{\rho}{a}\right)\exp(in\psi), \tag{33}$$

and the eigenvalues

$$\lambda_k \equiv \lambda_{n\mu} = \frac{D\beta_{n\mu}^2}{a^2}. \tag{34}$$

The radius ρ and polar angle ψ define the two-dimensional radius-vector $\boldsymbol{\rho}$ in the polar coordinate system, the $J_n(x)$ are the Bessel functions ($n = 0, \pm1, \pm2, \ldots$), and $\beta_{n\mu}$ ($\mu = 0,\ 1,\ 2, \ldots$) are nonnegative roots of the equation $J_n'(x) = 0$. The normalization factor $\eta_{n\mu}$ determined by the condition [9] is equal to

$$\eta_{ns} = \left[\left(1 - \frac{n^2}{\beta_{n\mu}^2}\right)\cdot J_n^2(\beta_{n\mu})\right]^{-1/2}. \tag{35}$$

TABLE 1
Roots of the Equations $J_n'(x) = 0$ (2D Model) and $j_n'(x) = 0$ (3D Model) in Ascending Order

			$\beta_{n\mu}$	
k	n	μ	2D	3D
0	0	0	0	0
1	1	0	1.8412	2.0816
2	2	0	3.0542	3.3421
3	0	1	3.8317	4.4934
4	3	0	4.2012	4.5141
5	4	0	5.3175	5.6467
6	1	1	5.3314	5.9404
7	5	0	6.4156	6.7565
8	2	1	6.7061	7.2899
9	0	2	7.0156	7.7253

Thus, in the two-dimensional case the eigenfunctions $\{u_k\}$ are numerated by two indices, $k = (n, \mu)$. For numerical calculations based on Eq. [14] one should find roots of the transcendental equation $J_n'(x) = 0$ for different n, arrange the roots in ascending order, and choose first M of them, where M is a chosen dimensionality of the matrices $\hat{\mathbf{U}}$ and $\hat{\mathbf{\Lambda}}$. The first 10 roots (in ascending order) with corresponding values of k, n, and μ are given in Table 1.

It should be noted that the roots corresponding to the Bessel function of orders n and $-n$ are degenerate, $\beta_{n\mu} = \beta_{-n\mu}$. This fact makes it possible to facilitate numerical calculations and shorten the dimensionality M of the matrices $\hat{\mathbf{U}}$ and $\hat{\mathbf{\Lambda}}$ (while delivering the same accuracy in the signal). For this purpose it is convenient to use the linear combinations of the eigenfunctions [33] with opposite n,

$$u_{n\mu}^{(+)}(\boldsymbol{\rho}, t) = \tilde{\eta}_{n\mu}\, J_n\left(\beta_{n\mu}\frac{\rho}{a}\right)\cos n\psi,$$
$$u_{n\mu}^{(-)}(\boldsymbol{\rho}, t) = \tilde{\eta}_{n\mu}\, J_n\left(\beta_{n\mu}\frac{\rho}{a}\right)\sin n\psi, \qquad [36]$$

where $\tilde{\eta}_{0\mu} = \eta_{0\mu}$ and $\tilde{\eta}_{n\mu} = \eta_{n\mu}\sqrt{2}$ for $n \neq 0$. In this case, the index n runs over only nonnegative integers, but the eigenfunctions with $n \neq 0$ are numerated not by two but three indices, $k = (n, \mu, \pm)$. However, it turns out that the components of the vector $\mathbf{F}$ corresponding to $u_{n\mu}^{(-)}$ are equal to 0, whereas the matrix $\hat{\mathbf{U}}$ is diagonal over the indices + and −. Therefore all terms connected with $u_{n\mu}^{(-)}$ do not contribute to the matrix product in Eq. [14], and we can operate with only the functions $u_{n\mu}^{(+)}$.

Substituting the eigenfunctions [33] in Eqs. [11] and [13], for the constant field gradient G applied in the circle's plane (XY) in an arbitrary direction (let it be X, i.e., $H = Gx = G\rho\cos\psi$), we obtain the components of the vector $\mathbf{F}$ and of the matrix $\hat{\mathbf{U}}$:

$$F_k \equiv F_{n\mu} = \frac{\tilde{\eta}_{n\mu}}{\pi a^2}\int_0^a \rho d\rho \int_0^{2\pi} d\psi \exp(i Q\rho\cos\psi)\cdot J_n\left(\beta_{n\mu}\frac{\rho}{a}\right)\cos n\psi$$
$$= 2(-i)^n\tilde{\eta}_{n\mu}\left[\frac{\Phi J_{n-1}(\Phi)J_n(\beta_{n\mu}) - \beta_{n\mu}J_n(\Phi)J_{n-1}(\beta_{n\mu})}{\left(\beta_{n\mu}^2 - \Phi^2\right)}\right], \qquad [37]$$

$$U_{k_1k_2} \equiv U_{n_1\mu_1,n_2\mu_2} = \frac{\tilde{\eta}_{n_1\mu_1}\tilde{\eta}_{n_2\mu_2}}{\pi a^2}\int_0^a \rho d\rho \int_0^{2\pi} d\psi \exp(i Q\rho\cos\psi)$$
$$\cdot J_{n_1}\left(\beta_{n_1\mu_1}\frac{\rho}{a}\right)\cos n_1\psi\, J_{n_2}\left(\beta_{n_2\mu_2}\frac{\rho}{a}\right)\cos n_2\psi$$
$$= \tilde{\eta}_{n_1\mu_1}\tilde{\eta}_{n_2\mu_2}\cdot\left[(-i)^{n_2+n_1}W_{k_1k_2}^{+}(\Phi) + (-i)^{n_2-n_1}W_{k_1k_2}^{-}(\Phi)\right], \qquad [38]$$

where $W^{\pm}$ are given by

$$W_{k_1k_2}^{\pm}(\Phi) = \int_0^1 x dx\, J_{n_2\pm n_1}(Qx)J_{n_1}\left(\beta_{n_1\mu_1}x\right)J_{n_2}\left(\beta_{n_2\mu_2}x\right) \qquad [39]$$

with $\Phi = Qa = \gamma Ga\Delta t$.

An analog of the *sinc*-function describing the FID signal in the static dephasing regime ($p = 0$) for the 2D model has the form

$$s(\tau) = \frac{2J_1(\tau)}{\tau}, \qquad p = 0. \qquad [40]$$

In the Gaussian approximation the FID signal is described by an expression similar to Eq. [30]:

$$s^{(G)}(\tau) = \exp\left[-\frac{2}{p^2}\sum_{\mu=0}^{\infty}\frac{g\left(p\beta_{1\mu}^2\tau\right)}{\beta_{1\mu}^6\left(\beta_{1\mu}^2 - 1\right)}\right]. \qquad [41]$$

Here $\beta_{1\mu}$ are the positive roots of the equation $J_1'(x) = 0$ and the function $g(x)$ is given by Eq. [31].

5. THE 3D MODEL

The solution of the three-dimensional diffusion equation [6] within a sphere of radius a, satisfying the boundary condition $(\partial P/\partial r)_{|r=a} = 0$, can be written in the form [8] with the eigenfunctions (*31*)

$$u_k(\mathbf{r}, t) \equiv u_{nm\mu}(\mathbf{r}, t) = \eta_{nm\mu}\, j_n\left(\beta_{n\mu}\frac{r}{a}\right)P_n^{|m|}(\cos\theta)\exp(im\psi), \qquad [42]$$

and the eigenvalues

$$\lambda_k \equiv \lambda_{n\mu} = \frac{D\beta_{n\mu}^2}{a^2}. \qquad [43]$$

Here the radius r and polar and azimuth angles θ and ψ define the three-dimensional radius-vector $\mathbf{r}$ in spherical coordinates, the $j_n(x)$ are the spherical Bessel functions ($n = 0, 1, 2, \ldots$), the $\beta_{n\mu}(\mu = 0, 1, 2, \ldots)$ are the nonnegative roots of the equations $j_n'(x) = 0$, and the $P_n^m(x)$ ($|m| \le n$) are the associated Legendre polynomials. The normalization factor $\eta_{nm\mu}$ determined by the condition [9] is equal to

$$\eta_{nm\mu} = \left[\frac{2(2n+1)(n-|m|)!}{3(n+|m|)!}\frac{\beta_{n\mu}^2}{\left[\beta_{n\mu}^2 - n(n+1)\right]j_n^2(\beta_{n\mu})}\right]^{1/2}. \qquad [44]$$

Thus, in the three-dimensional model the eigenfunctions $\{u_k\}$ are numerated by three indices, $k = (n, m, \mu)$. As in the 2D model described in the previous section, for numerical calculations based on Eq. [14] one should find roots of the transcendental equations $j_n'(x) = 0$ for different n, arrange the roots in ascending order, and select the first M of them, where M is a chosen dimensionality of the matrices $\hat{\mathbf{U}}$ and $\hat{\mathbf{\Lambda}}$ (note that these roots are degenerate with respect to the azimuth index m). The values of the indices n, μ corresponding to the first 10 roots in the 3D model (arranged in ascending order) are the same as in the 2D model discussed above, therefore they are given in the same Table 1.

Substituting the eigenfunctions [42] in Eq.[11], for a constant field gradient G applied in an arbitrary direction (let it be Z, i.e., $H = Gz = Gr\cos\theta$), we obtain the components of the vector $\mathbf{F}$,

$$\begin{aligned} F_k \equiv F_{nm\mu} &= \frac{3\eta_{nm\mu}}{4\pi a^3}\int_0^a r^2\,dr\int_0^\pi \sin\theta\,d\theta\int_0^{2\pi} d\psi \\ &\times \exp(iQr\cos\theta)\cdot j_n\left(\beta_{n\mu}\frac{r}{a}\right)P_n^{|m|}(\cos\theta)\exp(im\psi) \\ &= 3i^n\eta_{n0\mu}\left[\frac{\Phi j_{n-1}(\Phi)j_n(\beta_{n\mu}) - \beta_{n\mu}j_n(\Phi)j_{n-1}(\beta_{n\mu})}{\left(\beta_{n\mu}^2 - \Phi^2\right)}\right]\cdot\Delta_{m,0}, \end{aligned} \qquad [45]$$

where Δ_{mn} is the Kronecker delta. Thus, only components of the vector $\mathbf{F}$ corresponding to $m = 0$ differ from zero. It can also be easily shown that the matrix $\hat{\mathbf{U}}$ is diagonal with respect to the azimuth index m, $U_{n_1m_1\mu_1,n_2m_2\mu_2} \sim \Delta_{m_1,m_2}$. Consequently, all terms connected with the eigenfunctions u_k with $m \neq 0$ do not contribute to the matrix product in Eqs. [14]–[18], and we will further operate only with the eigenfunctions with $m = 0$, omitting the azimuth index m in all expressions.

Substituting the eigenfunctions [42] with $m = 0$ in Eq. [13] and making use of the formula (32)

$$\begin{aligned} P_{n_1}(x)P_{n_2}(x) &= \sum_{l=0}^{\min\{n_1n_2\}} C_{n_1n_2l}P_{n_1+n_2-2l}(x), \\ C_{n_1n_2l} &= \frac{a_{n_1-l}a_{n_2-l}a_l}{a_{n_1+n_2-l}}\cdot\frac{(2n_1+2n_2-4l+1)}{(2n_1+2n_2-2l+1)}, \\ a_p &= \frac{(2p-1)!!}{p!}, \end{aligned} \qquad [46]$$

we obtain the elements of the matrix $\hat{\mathbf{U}}$ in the sphere model,

$$\begin{aligned} U_{k_1k_2} &\equiv U_{n_1\mu_1,n_2\mu_2} \\ &= \frac{3\eta_{n_1\mu_1}\eta_{n_2\mu_2}}{4\pi a^3}\int_0^a r^2dr\int_0^\pi \sin\theta\,d\theta\int_0^{2\pi} d\psi\,\exp(iQr\cos\psi) \\ &\quad\cdot j_{n_1}\left(\beta_{n_1\mu_1}\frac{r}{a}\right)P_{n_1}(\cos\theta)j_{n_2}\left(\beta_{n_2\mu_2}\frac{r}{a}\right)P_{n_2}(\cos\theta) \\ &= 3\eta_{n_1\mu_1}\eta_{n_2\mu_2}\sum_{l=0}^{\min\{n_1,n_2\}} C_{n_1n_2l}i^{n_1+n_2-2l}V_{k_1k_2l}(Q), \end{aligned} \qquad [47]$$

$$V_{k_1k_2l}(Q) = \int_0^1 x^2dx\; j_{n_1+n_2-2l}(Qx)j_{n_1}\left(\beta_{n_1\mu_1}x\right)j_{n_2}\left(\beta_{n_2\mu_2}x\right), \qquad [48]$$

where $\Phi = Qa = \gamma Ga\,\Delta t$.

An analog of the *sinc*-function describing the FID signal in the static dephasing regime ($p = 0$) for the 3D model has the form

$$s(\tau) = \frac{3j_1(\tau)}{\tau} = \frac{3}{\tau^3}(\sin\tau - \tau\cos\tau), \qquad p = 0. \qquad [49]$$

In the Gaussian approximation the FID signal is described by the expression similar to Eq. [30],

$$s^{(G)}(\tau) = \exp\left[-\frac{2}{p^2}\sum_{\mu=0}^{\infty}\frac{g\left(p\beta_{1\mu}^2\tau\right)}{\beta_{1\mu}^6\left(\beta_{1\mu}^2 - 2\right)}\right], \qquad [50]$$

where the $\beta_{1\mu}$ are the positive roots of the equation $j_1'(x) = 0$ and the function $g(x)$ is given in Eq. [31].

6. RESULTS AND DISCUSSION

As mentioned above, for numerical calculations in the framework of RWA, we need to choose two quantities: the time-step Δt and the matrix dimension M. The first value should be chosen such that Δt will be much less than both the characteristic times: $\Delta t \ll t_D$ and $\Delta t \ll t_c$. If $p \le 1$, then the condition $\Delta t \ll t_c$ is stricter and the dimensionless interval $\Delta\tau = \Delta t/t_c = 1/20$ turns out to be sufficiently small for calculating the signal with an accuracy of 0.5%. For $p > 1$, the inequality $\Delta\tau \ll 1/p$ must hold; for example, for $p = 2$ this accuracy is achieved at $\Delta\tau \approx 1/50$. The matrix dimension M is determined by the k-dependence of the matrix elements Λ_{kk}, which decrease exponentially,

$\Lambda_{kk} = \exp(-p\beta_k^2\tau)$, therefore smaller p's require larger M. Our calculations showed that in the interval $\tau < 20$ the accuracy 0.5% is achieved at $M = 10$ for $p < 0.1$. For $0.1 < p < 1$ one can choose $M = 5$, and $M = 3$ is enough for $p > 1$. In what follows, we display numerical results calculated according to the above-described criteria.

General Features of MR Signal

The FID signal for the 1D model is plotted in Fig. 1 for several values of the parameter p. The curves corresponding to small p (0, 0.05, 0.1) demonstrate oscillating behavior whereas the curve for $p = 0.5$ is monotone. In more detail the evolution of the 1D FID signal behavior with increasing parameter p is shown in Fig. 2 in a logarithmic scale (solid lines). Deep minima of $\ln|s(\tau)|$ correspond to roots of $s(\tau)$ and obviously tend to $-\infty$. For small p, the behavior of the signal is similar to the oscillating behavior in the static dephasing regime (see Eq. [29]); the roots of the function $s(\tau)$ are arranged approximately equidistantly, therefore we can speak about a "period" of the oscillations. With p increasing, the "period" of the oscillations increases, the roots of $s(\tau)$ shifting to higher values of τ. For $p \geq 0.45$ the minima disappear, which means the function $s(\tau)$ becomes monotone. In this monotone regime the slope of the curves in Fig. 2 decreases with p increasing—a manifestation of the motional narrowing effect.

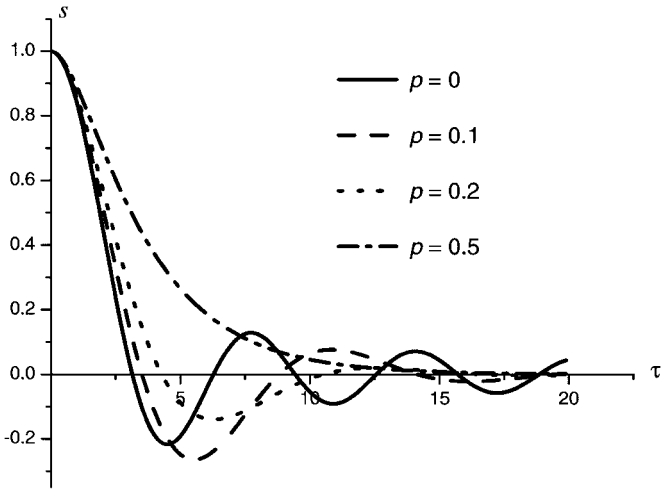

FIG. 1. The FID signal $s(t)$ in the 1D model. Times are expressed in dimensionless units, $\tau = t/t_c$, with t_c being the characteristic dephasing time, $t_c = (\gamma G a)^{-1}$. The parameter p is $t_c/t_D = D/(\gamma G a^3)$. The transition between the static case with oscillating FID signal to the motional narrowed case with monotonic signal is evident between $p = 0.2$ and 0.5.

There are three possible ways for the transformation from oscillating to monotone behavior of the function $s(\tau)$ to occur: (1) the "period" of the oscillations increases with p increasing and asymptotically tends to infinity at $p \to \infty$; (2) the "period"

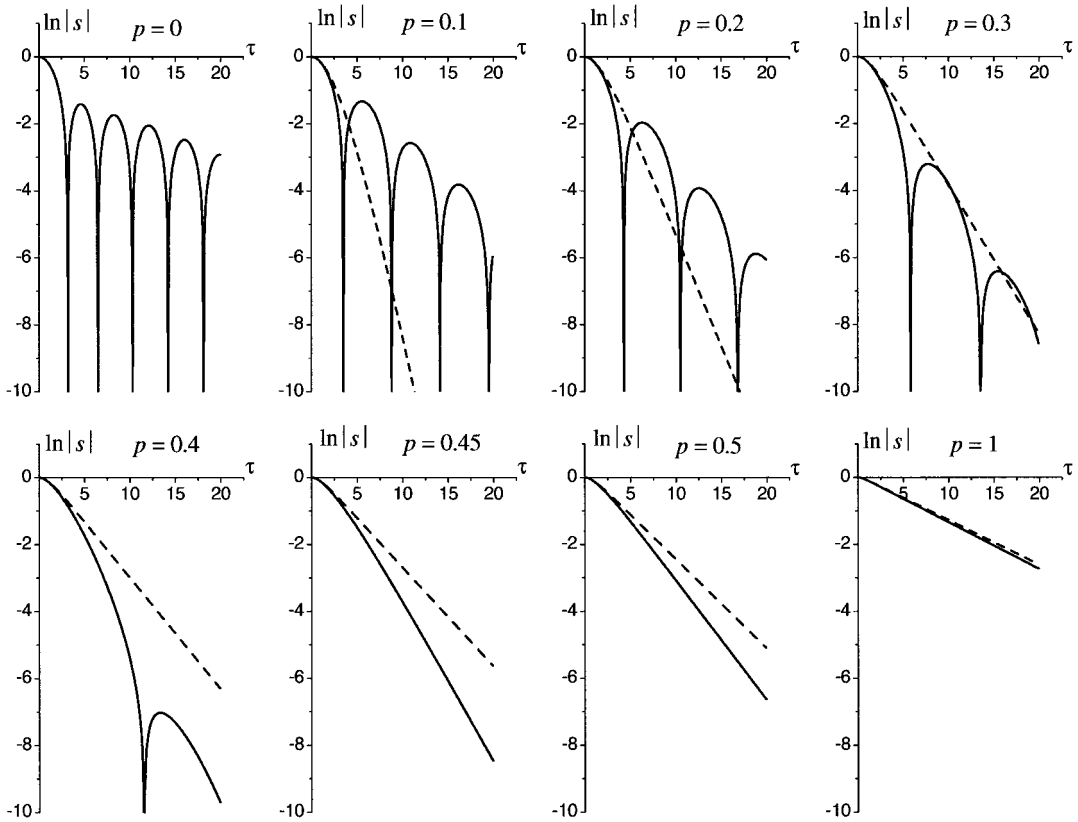

FIG. 2. The FID signal (logarithmic scale) in the 1D model for different values of the parameter $p = t_c/t_D$. Nearly periodic oscillating behavior is present for $p \leq 0.4$ with period increasing with increasing p. For $p > 0.45$, a monotonic decay is evident. The dashed curves show the Gaussian phase approximation.

of the oscillations tends to infinity at a certain finite bifurcation point $p = p_c$; (3) there is a set of bifurcation points, in which roots $\tau_n (n = 1, 2, \ldots)$ of the equation $s(\tau) = 0$ disappear by pairs. To determine how the transformation actually occurs, we numerically analyze the dependence of the roots τ_n on the parameter p. Figure 3 shows the p-dependence of the smallest root τ_1 (the p-dependence of the other roots is similar). For $p = 0$, we have $\tau_n = n\pi$ (see Eq. [29]); with increasing p all roots also increase, remaining approximately equidistant, and at $p = p_c \approx 0.443$ all τ_n tend to infinity. It means that there is a single bifurcation point $p_c = 0.443$, where the "period" of oscillation of the FID signal $s(\tau)$ becomes infinite and monotone behavior of the FID signal sets in (case 2). The dashed lines in Fig. 2 display the FID signal calculated in the framework of the Gaussian phase approximation (see Eq. [30]).

The logarithm of the SE signal in the 1D model, calculated on the basis of Eq. [18], is illustrated in Fig. 4 for the same values of the parameter p as in Fig. 2 for the FID signal. In the static dephasing regime ($p = 0$), we obtain $s_{SE} = 1$; we therefore substituted this trivial graph by that for $p = 0.01$. For all p the dependence of the $\ln(s_{SE}(\tau))$ on τ is monotone; however, in the interval $0.1 \le p \le 0.3$ there are characteristic oscillations of its derivative with respect to τ. As for the FID signal, the "period" of these oscillations increases as p increases, and for $p > 0.4$ the oscillations disappear. The Gaussian approximation adequately describes the SE signal in the short-time interval for small values of p and in the motional narrowing regime ($p \ge 1$).

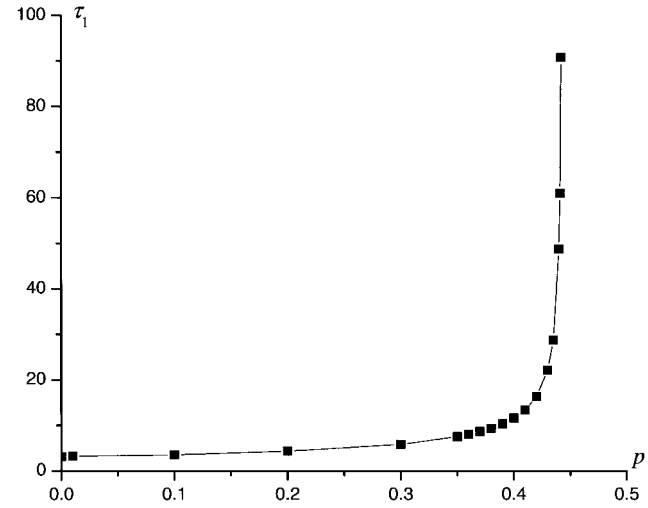

FIG. 3. The dependence of the lowest root (τ_1) of the equation $s(\tau) = 0$ in the 1D model on the parameter $p = t_c/t_D$. At the bifurcation point $p = 0.443$ τ_1 (as well as all other roots of this equation) tends to infinity and the signal $s(\tau)$ becomes a monotone function.

In Figs. 5 and 6 we plot $\ln(|s(\tau)|)$ for the FID signal in the 2D and 3D models, respectively (solid lines), along with the

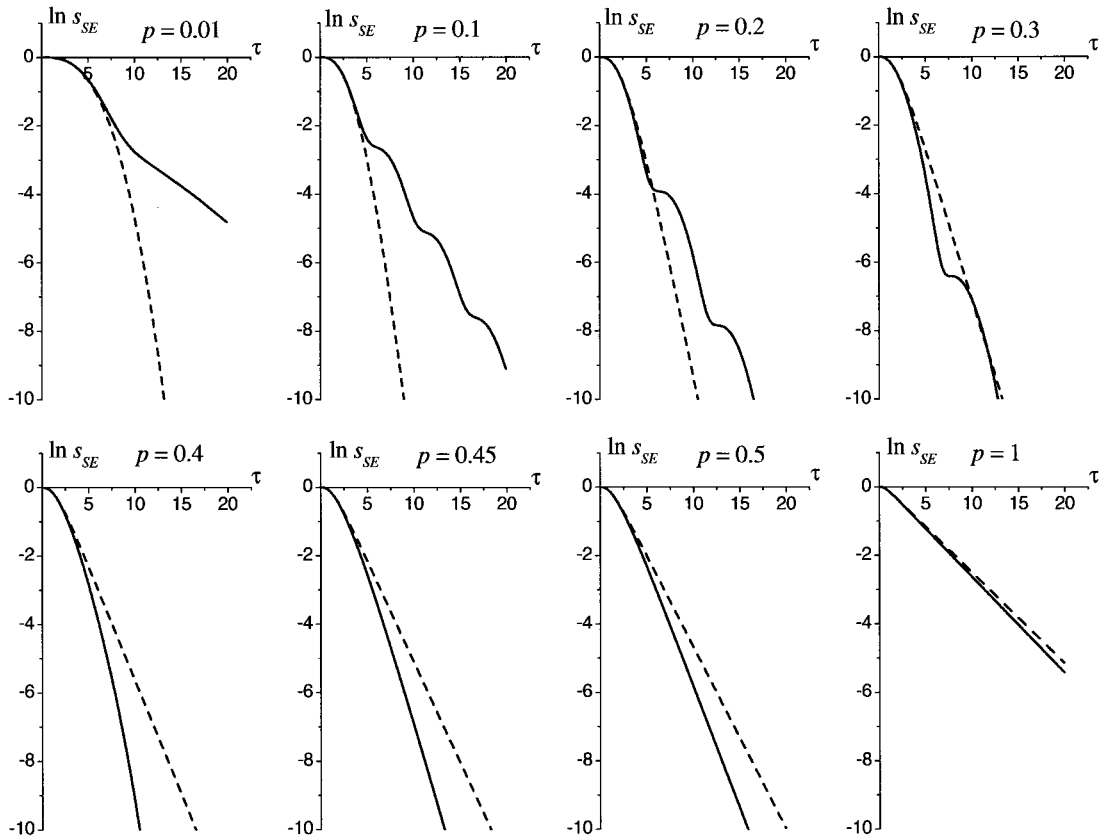

FIG. 4. The SE signal (logarithmic scale) in the 1D model for the same values of the parameter $p = t_c/t_D$ as in Fig. 2 for the FID signal. While the echo amplitude decay is always monotonic, oscillatory variations in the slope appear for $p \le 0.3$.

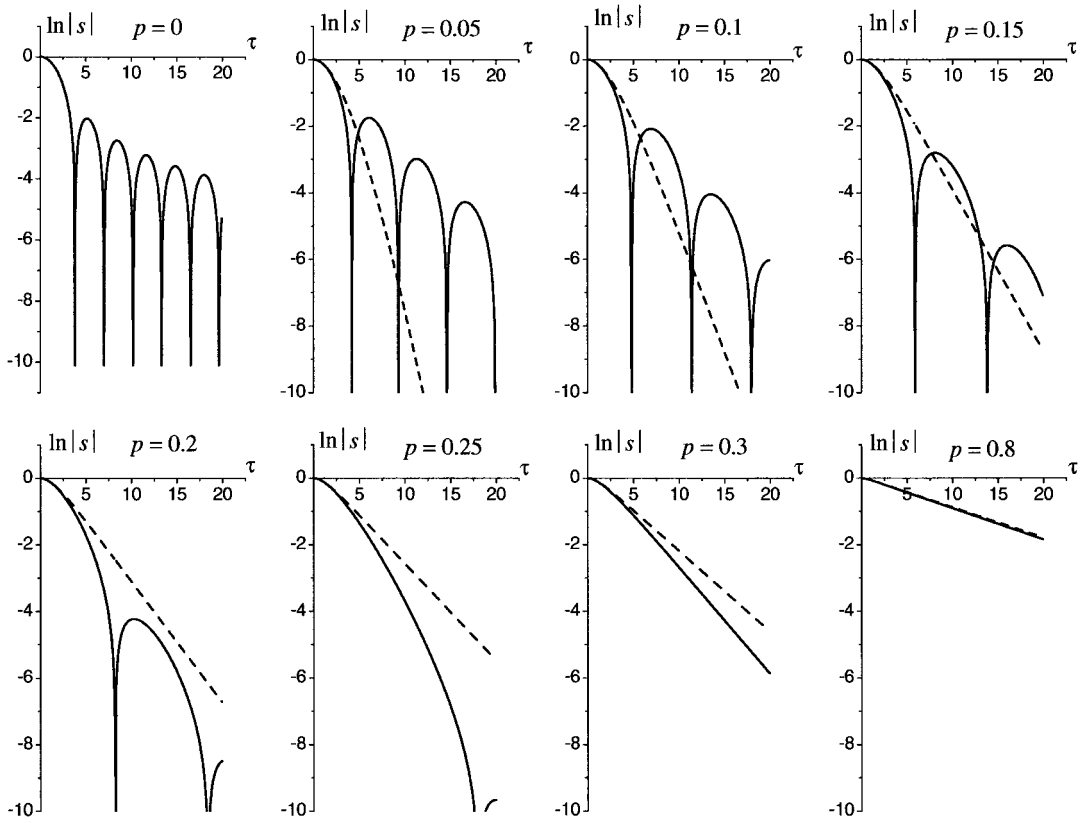

FIG. 5. The FID signal (logarithmic scale) in the 2D model for different values of the parameter $p = t_c/t_D$. The oscillating behavior is present for $p < 0.3$.

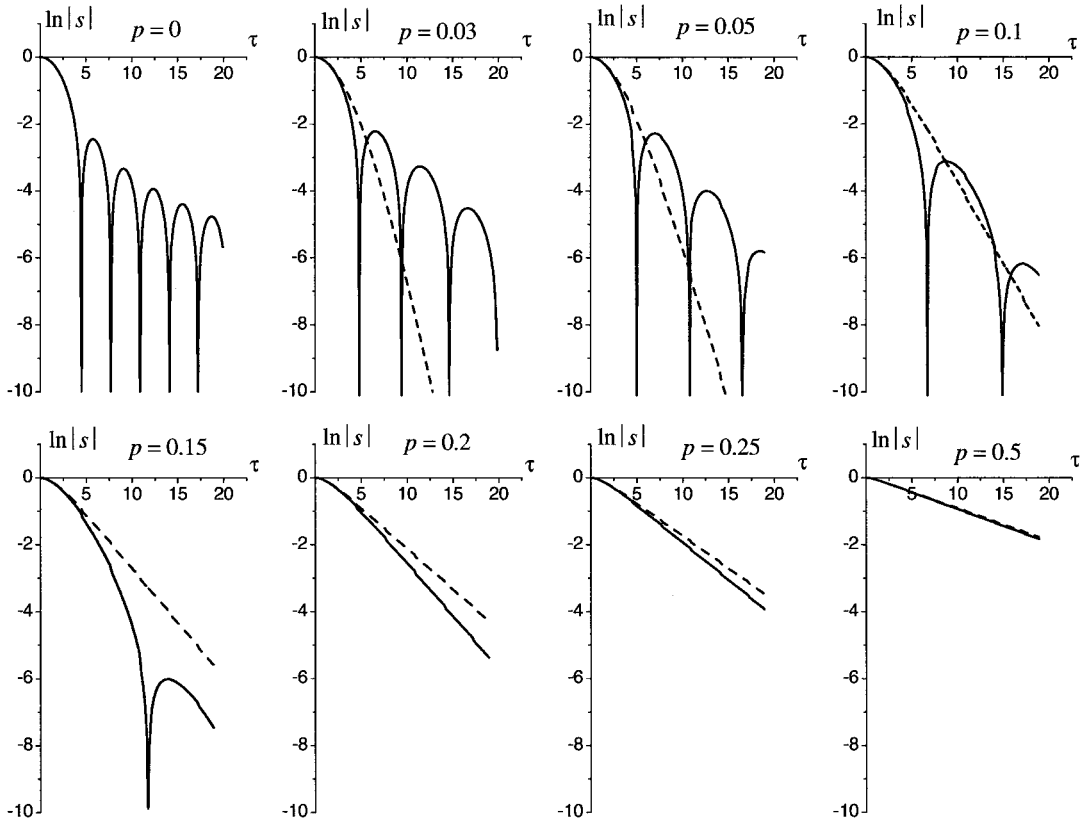

FIG. 6. The FID signal (logarithmic scale) in the 3D model for different values of the parameter $p = t_c/t_D$. The oscillating behavior is present for $p < 0.2$.

corresponding results of the Gaussian approximation (dashed lines). The general features of these graphs are the same as for the 1D model. In the static dephasing regime, when the signals are described by Eqs. [40] and [49], and for small p-value, the FID signal oscillates, the distances between roots of the function $s(t)$ increasing as p increases. The transition from the oscillating behavior to the monotone one takes place for smaller values of the parameter p than in the 1D model: the oscillations disappear at the bifurcation point $p_c \approx 0.27$ in the 2D model and $p_c \approx 0.17$ in the 3D model.

Thus, the evolution of the FID signal from static dephasing-like behavior to the motional narrowing regime in the 2D and 3D model is "faster" than in the 1D model. This result should be expected because one-dimensional diffusion along the field gradient in a sphere is effectively more restricted than in a circle, which in its turn is more restricted than in a segment.

Gaussian Approximation

As seen from Figs. 2, 4–6, the signals predicted by the Gaussian approximation for small p-values coincide with the exact results in the short-time regime. As p increases and oscillations in the time-dependence of the signals disappear, the discrepancy between solid and dashed curves progressively narrows, and for $p \geq 1$ in the 1D model the Gaussian approximation becomes an adequate approach for all time intervals, as expected. In the 2D and 3D models, the Gaussian approximation becomes adequate in all time intervals for $p \sim 0.8$ and $p \sim 0.5$, respectively.

A qualitative comparison of the exact results obtained in the framework of RWA with those obtained in the Gaussian phase approximation can be made by visual comparison of the solid and dashed curves in Figs. 2 and 4–6. To estimate quantitatively the applicability of the Gaussian approximation, we compute the relative error

$$\varepsilon = \big(s(\tau) - s^{(G)}(\tau)\big)\big/ s(\tau) \qquad [51]$$

at the time τ, where the signal has decayed by a certain factor ν, $S(\tau)/S_0 = \nu$. In Tables 2 and 3 we provide the relative error (in %) made by the Gaussian approximation in comparison with the exact results at the times τ_{d1} and τ_{d2}, where $\nu_1 = e^{-1}$ and $\nu_2 = e^{-2}$, respectively, for the FID and SE signals in the 1D, 2D, and 3D models.

For the FID signal, the error monotonically decreases with increasing value of the parameter p, whereas the times τ_{d1} and τ_{d2} monotonically increase. A single exception is the 2D model, where $\varepsilon(\tau_{d1},\, p = 0.1) < \epsilon(\tau_{d1},\, p = 0.2)$. For the SE signal, the dependence of the error on p is nonmonotonic. It should be underlined, however, that the error for the SE signal at the time τ_{d1} does not exceed 7% even for the 1D model; this means that the Gaussian approximation is a rather good approach in the most important (from the experimental point of view) acquisition time interval, $\tau \leq \tau_{d1}$ (i.e., with substantial remaining signal amplitude).

Short- and Long-Time Approximations

Analytical expressions for both FID and SE signals can be obtained in some limiting cases. Consider first the case $t_D \leq t_c (p \geq 1)$. In the motional narrowing regime $t \gg t_D$, the behavior of the FID signal is similar to that for the SE signal because, due to fast diffusion, the 180° RF pulse cannot refocus the spin's phase and therefore does not substantially affect the signal. In this regime, both the FID and SE signals can be described within the framework of the Gaussian approximation.

TABLE 2
The Relative Error (in %) Made by the Gaussian Approximation as Compared to the Exact Results Obtained in the Framework of the Random Walk Approach for the FID Signal

	$s(\tau_{d1}) = e^{-1}$						$s(\tau_{d2}) = e^{-2}$					
	$\frac{s(\tau_{d1}) - s^{(G)}(\tau_{d1})}{s(\tau_{d1})}$, %			τ_{d1}			$\frac{s(\tau_{d2}) - s^{(G)}(\tau_{d2})}{s(\tau_{d2})}$, %			τ_{d2}		
p	1D	2D	3D	1D	2D	3D	1D	2D	3D	1D	2D	3D
0.1	23	16	14	2.4	3.0	3.7	131	94	78	3.1	4.0	5.3
0.2	23	17	10	2.7	3.7	5.1	118	70	33	3.6	5.4	8.7
0.3	22	13	6	3.1	4.6	7.0	89	40	13	4.3	7.9	13.1
0.4	18	9	3	3.5	5.8	9.1	68	21	7	5.5	10.7	17.5
0.5	15	6	2	4.1	7.1	11.2	45	13	4	7.0	13.5	21.9
0.6	11	4	1	4.7	8.4	13.4	29	9	3	8.5	16.3	26.3
0.7	9	3	1	5.4	9.8	15.5	21	6	2	10.1	19.1	30.7
0.8	7	2	0	6.1	11.1	17.7	16	5	1	11.7	21.8	35.1
0.9	6	2	0	6.9	12.5	19.9	12	4	0	13.2	24.6	39.5
1.0	5	1	0	7.6	13.8	22.1	10	3	0	14.7	27.3	44.0

Note. Separate results are given for times where the signal has decayed by $1/e$ and $1/e^2$. The parameter p is t_c/t_D. Times are expressed in dimensionless units, $\tau = t/t_c$.

TABLE 3
The Relative Error (in %) Made by the Gaussian Approximation as Compared to the Exact Results Obtained in the Framework of the Random Walk Approach for the SE Signal

	$s_{SE}(\tau_{d1}) = e^{-1}$						$s_{SE}(\tau_{d2}) = e^{-2}$					
	$\frac{s_{SE}(\tau_{d1}) - s_{SE}^{(G)}(\tau_{d1})}{s_{SE}(\tau_{d1})}$, %			τ_{d1}			$\frac{s_{SE}(\tau_{d2}) - s_{SE}^{(G)}(\tau_{d2})}{s_{SE}(\tau_{d2})}$, %			τ_{d2}		
p	1D	2D	3D	1D	2D	3D	1D	2D	3D	1D	2D	3D
0.1	3	1	3	6.4	6.8	7.2	24	10	18	9.0	9.0	9.8
0.2	2	5	5	5.6	6.4	7.4	17	26	19	9.8	9.1	11.4
0.3	6	6	4	5.6	6.6	8.6	28	23	11	7.6	10.2	14.8
0.4	7	6	3	5.6	7.4	10.2	32	17	6	8.2	12.3	18.7
0.5	7	5	2	5.8	8.4	12.2	28	12	4	9.0	14.8	22.7
0.6	7	3	1	6.2	9.4	14.2	23	8	2	10.2	17.2	27.0
0.7	6	3	1	6.6	10.6	16.2	18	6	2	11.4	20.0	31.3
0.8	5	4	0	7.2	11.8	18.2	14	5	1	12.8	22.5	35.6
0.9	4	2	0	7.8	13.2	22.4	11	4	0	14.2	25.1	40.0
1.0	4	1	0	8.4	14.3	22.5	9	3	0	15.6	28.0	44.4

Note. Separate results are given for times where the signal has decayed by $1/e$ and $1/e^2$. The parameter p is t_c/t_D. Times are expressed in dimensionless units, $\tau = t/t_c$.

In the long-time limit, $t \gg t_D$ ($p\tau \gg 1$), the arguments of the functions $g(x)$ [31] for the FID signal and $\bar{g}(x)$ [32] for the SE signal, entering Eqs. [30], [41], and [50], are large; therefore $g(x) \simeq \bar{g}(x) \simeq x$, the sums in Eqs. [30], [41], and [50] can be calculated exactly, and the signal can be written as

$$s(\tau) \simeq s_{SE}(\tau) \simeq \exp\left(-\zeta_d \frac{\tau}{p}\right) = \exp\left(-\zeta_d \frac{(\gamma G)^2 a^4 t}{D}\right), \quad [52]$$

where the numerical coefficient ζ_d is determined by the model dimensionality d:

$$\zeta_1 = 2/15, \qquad \zeta_2 = 7/96, \qquad \zeta_3 = 8/175 \qquad [53]$$

(for the SE signal, an expression similar to Eq. [52] was obtained in (*30*)). Note that $\zeta_3 < \zeta_2 < \zeta_1$; i.e., the signal decay rate decreases going from 1D to 2D to the 3D model. This result should be expected because the motional narrowing effect is stronger in the model of higher dimensionality, where diffusion along the field gradient is effectively more restricted.

In the short-time limit, $t \ll t_D \leq t_c (p\tau \ll 1)$, the functions $g(x)$ and $\bar{g}(x)$ can be approximated as $g(x) \simeq x^2/2$ and $\bar{g}(x) \simeq x^3/12$, respectively. The FID signal in this limiting case takes the form

$$s(\tau) \simeq \exp(-\xi_d \tau^2) = \exp\left[-\xi_d \left(\frac{t}{\gamma G a}\right)^2\right], \qquad [54]$$

with the coefficients ξ_d depending on the model dimensionality d:

$$\xi_1 = 1/6, \qquad \xi_2 = 1/8, \qquad \xi_3 = 1/10. \qquad [55]$$

Note that $\xi_3 < \xi_2 < \xi_1$, that means spin dephasing is faster in the system of lower dimensionality. The SE signal in the short-time limit is independent from the model dimensionality d and the system size a and is described by the classical expression (*33*),

$$s_{SE}(\tau) \simeq \exp\left(-\frac{1}{12} p\tau^3\right) = \exp\left[-\frac{1}{12}(\gamma G)^2 D t^3\right] \quad [56]$$

(general conditions of applicability of such a t^3-behavior of SE signal is discussed in (*34*)).

Thus, the behavior of the FID signal in the short-time limit differs considerably from that of the SE signal. This difference takes place not only if $t \ll t_D \leq t_c$ but also in the slow motion regime, when $t \ll t_c \leq t_D$. In this regime, the Gaussian approximation is adequate for all p-value, and the FID signal is described by parabola

$$s(\tau) \simeq 1 - \xi_d \tau^2 \qquad [57]$$

(this result can be readily obtained by expanding the exponent in Eq. [56] or the formulas for the case $p = 0$ [29], [40], and [49] in series in τ).

It should be mentioned that a parabolic time dependence in the short-time interval ($t \ll t_c, t_D$) is a general property of FID signal regardless of a specific system structure, as shown for particular cases in (*4, 9, 35*) and explained in (*5*).

Edge Enhancement Effect

Another important effect—the so-called edge enhancement effect (*36–41*)—also follows from our theoretical approach. The physical origin of this effect is that spin diffusion in the

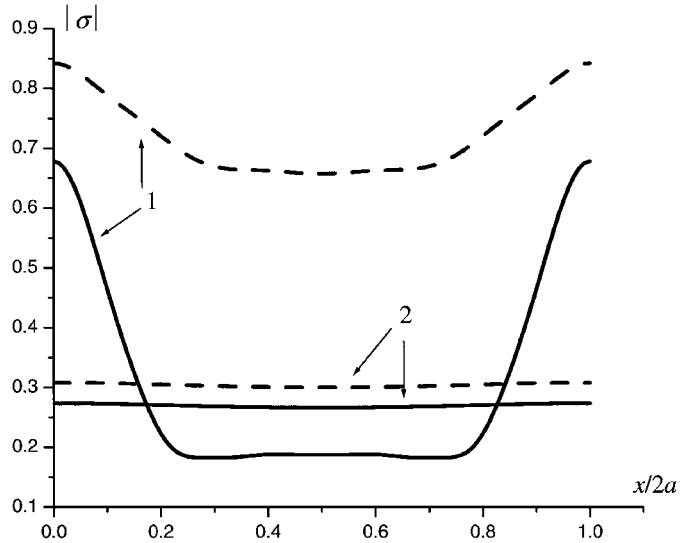

FIG. 7. The magnitude of the FID (solid lines) and SE (dashed lines) signal density $|\sigma|$ in the 1D model as a function of the dimensionless coordinate $(x/2a)$ for fixed time $\tau = t/t_c = 10$ and $p = 0.005$ (curves 1) and $p = 1$ (curves 2). The edge enhancement is pronounced in curves 1, when $t = 0.05\,t_D$, and is practically absent in curves 2, when $t = t_D$.

vicinity of system boundaries is effectively more restricted than that away from the boundaries. The edge enhancement effect is pronounced in the case, when two conditions are satisfied: (1) a characteristic diffusion distance $x_0 \sim (Dt)^{1/2}$ that a spin travels over time t is much smaller than a system size a, $x_0 \ll a$, or $t \ll t_D$; (2) the field gradient is strong enough to result in a substantial phase difference over x_0: $\gamma G x_0 t \gg 1$, i.e., $t \gg (t_c^2 t_D)^{1/3}$ (note that the combination in the right-hand side of the latter inequality is independent from the system size a). In dimensionless variables, these conditions are

$$p^{-1/3} \ll \tau \ll p^{-1}. \qquad [58]$$

Obviously, the double-inequality [58] can hold only for $p \ll 1$. In the case $t \geq t_D$, diffusion "stirs" all spins and the signal density becomes practically homogeneous at time t.

As mentioned in Section 2, the RWA makes it possible to calculate the signal density $\sigma(\mathbf{r}, t)$ produced by spins starting from a given space point $\mathbf{r}$ and the signal density $\sigma'(\mathbf{r}, t)$ from a given point $\mathbf{r}$, i.e., the signal from all spins ending their trajectory at $\mathbf{r}$ at time t (remind that $\sigma(\mathbf{r}, t) = \sigma'(\mathbf{r}, t)$). The magnitude $|\sigma|$ of the FID (solid lines) and SE (dashed lines) signal density for the 1D model is plotted in Fig. 7 as a function of the dimensionless coordinate $(x/2a)$ for two values of the parameter, $p = 0.005$ (curves 1) and $p = 1$ (curves 2) (time is fixed, $\tau = 10$). As expected, the curves 1 corresponding to $p = 0.005$ have pronounced maxima at the boundaries (at $x = 0$ and at $x = 2a$) whereas curves 2 are practically flat.

Biexponential Diffusion Attenuation

In the regime, when the edge enhancement effect can be observed, a general picture of the net signal is similar to that in a two-compartment system: one of the "compartments" comprises spins located far from the edges and their diffusion can be considered as unrestricted (fast-diffusion "compartment"). Diffusion of spins from the second "compartment," located in the vicinity of the boundaries (at distance $\sim (Dt)^{1/2}$), is more restricted due to encountering the boundaries (slow-difusion "compartment"). Therefore one can anticipate that the signal in this situation can be described by means of the *biexponential* function usually used for describing signals in two-compartment models,

$$s = f \exp(-bD_1) + (1 - f)\exp(-bD_2), \qquad [59]$$

where D_1 and D_2 are the apparent diffusion coefficients (ADC) in the compartments, f is the volume fraction of the first compartment, and b is the b-value determined by a gradient waveform. For the SE signal with the echo time t, $b = (\gamma G)^2 t^3/12$.

We compared the SE signal in the 1D model, obtained in the framework of RWA, with the biexponential function [59] by fitting s_{SE} as a function of the parameter b to Eq. [59] in the interval $bD < 10$ for several fixed dimensionless times $\tau' = t/t_D$. The results are summarized in Table 4. As we see, the biexponential function provides an excellent description of the theoretical curves $s_{SE}(b)$ for $\tau' \leq 1/6$. The "volume fraction" of the fast-diffusion "compartment" decreases with time because the number of spins encountering the boundaries increases. For higher $\tau'(\tau' > 1/6)$, the division of the system into "compartments" becomes meaningless: all the spins are stirred by diffusion and the signal cannot be described by the biexponential function [59]. For $\tau' \sim 1$ the signal dependence on the b-value becomes practically monoexponential. This regime corresponds to $t \sim t_D$, when all spins are stirred by diffusion and encounter the boundaries and the signal density is almost uniform (dashed curves in Fig. 7).

Thus, the close fit of experimental results to a biexponential function [59] is not sufficient to confirm the presence of two

TABLE 4

The Results of Fitting the Theoretically Calculated SE Signal in the 1D Model as a Function of the b-Value to the Biexponential Expression [59] for Different Dimensionless Time $\tau' = t/t_D$

$\tau' = t/t_D$	f	D_1	D_2	χ^2
1/50	0.94	0.851	0.141	$1.1 \cdot 10^{-7}$
1/20	0.91	0.842	0.117	$1.9 \cdot 10^{-7}$
1/10	0.89	0.778	0.104	$1.1 \cdot 10^{-7}$
1/6	0.86	0.706	0.092	$1.4 \cdot 10^{-7}$

Note. D_1 and D_2 are the fast and slow apparent diffusion coefficients, respectively, and f is the volume fraction of the fast-diffusion component; χ^2 is the statistical error.

disntinct physical compartments: indeed, in the presence of restrictive barriers both fast and slow terms in [59] can arise from the same physical compartment. This issue may be of interest for interpretation of experimental data in the brain tissue and other biological objects, where a biexponential diffusion attenuation of the MR signal for large b-value ($bD > 1$) has been observed (see, e.g., (*23–28*)) but has not been explained. Our results (biexponential behavior for large bD and small volume fraction corresponding to the slow-diffusion component) are in accordance with experimental data and demonstrate the importance of restrictive barriers. The important role of motional restrictions in explaining the origin of biexponential diffusion attenuation in tissue systems has also been demonstrated recently (*42*) by extensive computer simulations based on detailed anatomic images of axonal architecture.

7. CONCLUSIONS

We have presented a theoretical framework for analysis of the FID and SE signal behavior in the presence of magnetic field gradients. The FID signal time dependence in 1D, 2D, and 3D models of restricted diffusion is shown to depend crucially on the ratio between dephasing and diffusion characteristic times, $p = t_c/t_D$. For $p = 0$ (no diffusion, the static dephasing regime) and for small values of p the FID signal oscillates with time, the "period" of the oscillations increases with increasing p and tends to infinity at a bifurcation point $p = p_c$. The value of p_c decreases going from 1D to 2D to 3D. For $p > p_c$ the FID signal time dependence is monotonic and approaches a monoexponential function for $p \sim 1$ (motion narrowing regime). We have also provided a quantitative comparison of our results (for the FID signal as well as for the SE signal) with those obtained in the Gaussian phase approximation. Because the latter is broadly used for interpretation of experimental data, such a comparison can be useful for estimation of the corresponding error. Our approach makes it possible to analyze a space distribution of the signal density (transverse magnetization) and to demonstrate the edge enhancement effect. The presence of restrictive barriers in a one-compartment model can lead to a quasi-two-compartment behavior of the MR signal. This result suggests a simple rationale for the experimental findings of biexponential echo attenuation curves in MR diffusion experiments with tissue systems.

ACKNOWLEDGMENTS

The authors are grateful to Professors Mark S. Conradi and Joseph J. H. Ackerman for substantial and helpful comments and to Professor E. Fukushima for discussion. This work is supported in part by WU McDonnell Center for Higher Brain Function and the NIH Grant R01 NS4519-01A1.

REFERENCES

1. A. Abragam, "Principles of Nuclear Magnetism," Oxford Univ. Press, New York (1989).
2. P. T. Callaghan, "Principles of Nuclear Magnetic Resonance Microscopy," Claredon Press, Oxford (1991).
3. S. Ogawa, T. Lee, A. S. Nayak, and P. Glynn, Oxygenation-sensitive contrast in magnetic resonance image of rodent brain at high fields, *Magn. Reson. Med.* **14,** 68–78 (1990).
4. D. A. Yablonskiy and E. M. Haacke, Theory of NMR signal behavior in magnetically inhomogeneous tissues: The static dephasing regime, *Magn. Reson. Med.* **32,** 749–763 (1994).
5. A. L. Sukstanskii and D. A. Yablonskiy, Theory of FID NMR signal dephasing induced by mesoscopic magnetic field inhomogeneities in biological systems, *J. Magn. Reson.* **151,** 107–117 (2001).
6. V. G. Kiselev and S. Posse, Analytical model of susceptibility-induced MR signal dephasing: Effect of diffusion in a microvascular network, *Magn. Reson. Med.* **41,** 499–509 (1999).
7. V. G. Kiselev and S. Posse, Analytical theory of susceptibility induced NMR signal dephasing in a celebrovascular network, *Phys. Rev. Lett.* **81,** 5696–5699 (1998).
8. R. P. Kennan, J. Zhong, and J. C. Gore, Intravascular susceptibility contrast mechanisms in tissues, *Magn. Reson. Med.* **31,** 9–21 (1994).
9. L. A. Stables, R. P. Kennan, and J. C. Gore, Asymmetric spin-echo imaging of magnetically inhomogeneous systems: Theory, experiment, and numerical studies, *Magn. Reson. Med.* **40,** 432–442 (1998).
10. J. C. Ford, F. W. Wehrli, and H. W. Chung, Magnetic field distribution in models of trabecular bone, *Magn. Reson. Med.* **30,** 373–379 (1993).
11. R. M. Weisskopf, C. S. Zuo, J. L. Boxerman, and B. R. Rosen, Microscopic susceptibility variation and transverse relaxation: Theory and experiment, *Magn. Reson. Med.* **31,** 601–610 (1994).
12. J. L. Boxerman, L. M. Hamberg, B. R. Rosen, and R. M. Weisskoff, MR contrast due to intravascular magnetic susceptibility perturbations, *Magn. Reson. Med.* **34,** 555–566 (1995).
13. H. C. Torrey, Bloch equations with diffusion terms, *Phys. Rev.* **104,** 563–565 (1956).
14. V. M. Kenkre, E. Fukushima, and D. Sheltraw, Simple solution of the Bloch–Torrey equations in the NMR study of molecular diffusion, *J. Magn. Reson.* **128,** 62–69 (1997).
15. S. D. Stoller, W. Happer, and F. J. Dyson, Transverse spin relaxation in inhomogeneous magnetic field, *Phys. Rev. A* **44,** 7459–7477 (1991).
16. A. Caprihan, L. Z. Wang, and E. Fukushima, A multiple-narrow-pulse approximation for restricted diffusion in a time-varying field gradient, *J. Magn. Reson. A* **118,** 94–102 (1995).
17. P. T. Callaghan, A simple matrix formalism for spin echo analysis of restricted diffusion under generalized gradient waveform, *J. Magn. Reson.* **129,** 74–84 (1997).
18. S. L. Codd and P. T. Callaghan, Spin echo analysis of restricted diffusion under generalized gradient waveforms: Planar, cylindrical, and spheres pores with wall relaxivity, *J. Magn. Reson.* **137,** 358–372 (1999).
19. B. Balinov, B. Jonsson, P. Linse, and O. Soderman, The NMR self-diffusion method applied to restricted diffusion: Simulation of echo attenuation from molecules in spheres and between planes, *J. Magn. Reson. A* **104,** 17–25 (1993).
20. A. Coy and P. T. Callaghan, *J. Chem. Phys.* **101,** 4599 (1994).
21. M. H. Blees, The effect of finite duration of gradient pulses on the pulsed-field-gradient NMR method for studying restricted diffusion, *J. Magn. Reson. A* **109,** 203–209 (1994).
22. P. Linse and O. Soderman, The validity of the short-gradient-pulse approximation in NMR studies of restricted diffusion: Simulation of molecular diffusing between planes, in cylinders and spheres, *J. Magn. Reson. A* **116,** 77–86 (1995).
23. T. Niendorf, R. M. Dijkhuisen, D. G. Norris, M. van Lookeren Campagne, and K. Nicolay, Biexponential diffusion attenuation in various states of brain

tissue: Implications for diffusion-weighted imaging, *Magn. Reson. Med.* **36,** 847–857 (1996).

24. Y. Assaf and Y. Cohen, Non-mono-exponential attenuation of water and *N*-acetyl aspartate signals due to diffusion in brain tissue, *J. Magn. Reson.* **131,** 69–85 (1998).
25. D. L. Buckley, J. D. Bui, M. I. Phillips, T. Zelles, B. A. Inglis, H. D. Plant, and S. J. Blackband, The effect of ouabain on water diffusion in the rat hippocampal slice measured by high resolution NMR imaging, *Magn. Reson. Med.* **41,** 137–142 (1999).
26. B. A. Inglis, E. L. Bossart, D. L. Buckley, E. D. Wirth 3rd, and T. H. Mareci, Visualisation of neural tissue water compartment using biexponential diffusion tensor MRI, *Magn. Reson. Med.* **45,** 580–587 (2001).
27. C. A. Clark and D. Le Bihan, Water diffusion compartmentation and anisotropy at high b values in the human brain, *Magn. Reson. Med.* **44,** 852–859 (2000).
28. J. V. Sehy, J. J. H. Ackerman, and J. J. Neil, Evidence that both "fast" and "slow" water ADC components arise from the intracellular space, *in* "ISMRM-2002," Honolulu (2002).
29. B. Robertson, Spin-echo decay of spins diffusion in a bounded region, *Phys. Rev.* **151,** 273–277 (1966).
30. C. H. Neuman, Spin echo of spins diffusion in a bounded medium, *J. Chem. Phys.* **60,** 4508–4511 (1973).
31. H. S. Carslaw and J. C. Jaeger, "Conduction of Heat in Solids," 2nd ed., Claredon Press, Oxford (1959).
32. I. S. Gradstein and I. M. Ryzhik, "Table of Integrals, Series, and Products," 5th ed., Academic Press, New York (1999).
33. H. Y. Carr and E. M. Purcell, Effects of diffusion on free precession in nuclear magnetic resonance experiments, *Phys. Rev.* **94,** 630–638 (1954).
34. D. W. Pfitsch, A. F. McDowell, and M. S. Conradi, What are the conditions for exponential time-cubed echo decays? *J. Magn. Reson.* **139,** 364–370 (1999).
35. D. A. Yablonskiy, Quantitation of intrinsic magnetic susceptibility-related effects in a tissue matrix: Phantom study, *Magn. Reson. Med.* **39,** 417–428 (1998).
36. W. B. Hyslop and P. C. Lauterbur, Effects of restricted diffusion on microscopic NMR imaging, *J. Magn. Reson.* **94,** 501–510 (1991).
37. B. Putz, D. Barsky, and K. Schulten, Edge enhancement by diffusion in microscopic magnetic resonance imaging, *J. Magn. Reson.* **97,** 27–53 (1992).
38. P. T. Callaghan, A. Coy, L. C. Forde, and C. J. Rofe, Diffusive relaxation and edge enhancement in NMR microscopy, *J. Magn. Reson. A* **101,** 347–350 (1993).
39. T. M. de Swiet and P. N. Sen, Decay of nuclear magnetization by bounded diffusion in a constant field gradient, *J. Chem. Phys.* **100,** 5597–5604 (1994).
40. T. M. de Swiet, Diffusive edge enhancement in imaging, *J. Magn. Reson. B* **109,** 12–18 (1995).
41. B. Saam, N. Drukker, and W. Happer, Edge enhancement observed with hyperpolarized He-3, *Chem. Phys. Lett.* **263,** 481–487 (1996).
42. C. L. Chin, F. W. Wehrli, S. N. Hwang, M. Takahashi, and D. B. Hackney, Biexponential diffusion attenuation in the rat spinal cord: Computer simulations based on anatomic images of axonal architecture, *Magn. Reson. Med.* **47,** 455–460 (2002).